Hidden magnetic order on a kagome lattice for KV_3Sb_5

V. Scagnoli,[1,2] D. D. Khalyavin,[3] and S. W. Lovesey[3,4]

[1]*Laboratory for Mesoscopic Systems, Department of Materials, ETH Zurich, 8093 Zurich, Switzerland*
[2]*Laboratory for Multiscale Materials Experiments, Paul Scherrer Institute, 5232 Villigen PSI, Switzerland*
[3]*ISIS Facility, STFC, Didcot, Oxfordshire OX11 0QX, United Kingdom*
[4]*Diamond Light Source Ltd, Didcot, Oxfordshire OX11 0DE, United Kingdom*

(Received 25 May 2022; revised 24 July 2022; accepted 25 July 2022; published 12 August 2022)

KV_3Sb_5 has recently attracted considerable attention due to its low-temperature superconducting properties, which are heralded by a charge-density wave. The apparent presence of a very weak magnetism does not result in long-range ordering. An explanation of the properties we present invokes higher-order terms in the vanadium magnetization density and a "hidden order" of Dirac (polar) multipoles. The Dirac dipole, known as an anapole or toroidal dipole, is one of a family of electronic multipoles visible in x-ray and magnetic neutron diffractions while undetectable with standard laboratory-based techniques. Actually, two viable magnetic structures, direct descendants of the established chemical structure, are studied with a view to testing their suitability in future experiments. One model structure is magnetoelectric and restricted to the linear type, whereas a second model cannot show a magnetoelectric effect of any type. The latter hosts a strange vanadium entity that is a true scalar and magnetic (time-odd), and associated in our paper with a fictitious charge distribution that is purely imaginary. Calculated x-ray and neutron-scattering amplitudes are symmetry-informed expressions of vanadium Dirac multipoles. Bragg diffraction patterns for the two models are found to be distinctly different, fortunately. Likewise, magnetochiral signals derived from our x-ray scattering amplitudes.

DOI: 10.1103/PhysRevB.106.064419

I. INTRODUCTION

High-temperature superconductors are arguably among the most studied systems in solid-state physics. Decades after its first observation in a Ba-La-Cu-O system, there is still no consensus on its microscopic origin [1–3]. One hoary question is the relevance of orbital currents, once predicted to be the origin of the hidden phase of high-temperature cuprate superconductors as well as the origin of the quantum anomalous Hall effect [4–6]. Such currents run through the lattice breaking time-reversal symmetry, and there are recent reports suggesting their presence in the kagome (trihexagonal tiling) superconductors AV_3Sb_5 (A = K, Rb, and Cs) [7]. This family of compounds, which crystallizes in the hexagonal *P6/mmm* space group, has recently attracted a significant attention due to anomalies observed in its magnetic and electrical properties. At around a temperature $T^* \sim 100$ K changes in the electrical resistivity and magnetic susceptibility are observed [8,9]. Such anomalies have been associated with the development of a charge-density wave, whose response under an applied magnetic field points to the presence of chirality in the system [7]. This particular scenario uses an amalgam of $3q$ (quadruple) instabilities on a two-dimensional kagome lattice where it is energetically favorable for electrons to organize into a pattern of high and low concentrations (charge-density wave). Purely imaginary hopping parameters between the three sublattices creates a chiral flux ground state that responds to an applied magnetic field. Additionally, AV_3Sb_5 becomes superconducting in the 0.9–2.5 K temperature region [8,10,11]. Understandably, there are speculations on the exact nature of the electronic and magnetic state of AV_3Sb_5 below the temperature T^* associated with the development of the charge-density wave.

No magnetic order and concomitant time-reversal symmetry breaking has been revealed in KV_3Sb_5 to date. Powder neutron diffraction measurements find no obvious evidence of long-range or short-range magnetic ordering below 80 K [10]. In addition, Kenney *et al.*, find no evidence from muon spin rotation (μSR) and relaxation spectroscopy of a local vanadium V^{4+} magnetic moment [12]. However, weak internal magnetic fields are observed with zero-field μSR, and the authors speculate that it is due to simultaneous time-reversal and rotational symmetry breaking [13]. (Implanted muons occupy a variety of sites in a sample, and the origin of detected magnetic fields is speculation.) Here, we show that these experimentally determined properties can be reconciled in a magnetic structure not visible with standard experimental techniques. Notably, Bragg diffraction patterns gathered with a polarized neutron beam, or x-rays tuned in energy to a vanadium atomic resonance can validate our magnetic models for KV_3Sb_5. (Neutron polarization analysis offers a significantly higher sensitivity to magnetic scattering than the standard powder diffraction technique.) Scattering amplitudes for neutron and x-ray diffractions presented here have been calculated with crystal and magnetic symmetry tools.

In more detail, we assign Dirac multipoles on vanadium ions to address the enigmatic magnetic properties of KV_3Sb_5. They are polar (parity-odd) and magnetic (time-odd)

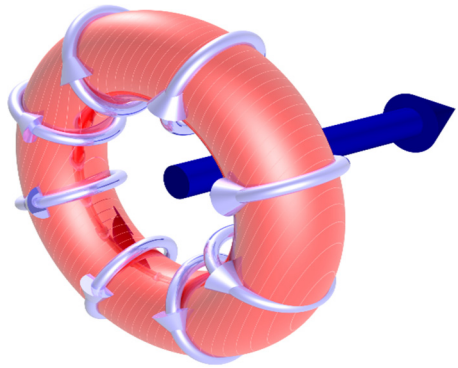

FIG. 1. Depiction of a toroidal dipole also known as an anapole.

electronic multipoles. An intra-unit-cell loop current order [13,16], likewise breaking both parity and time-reversal symmetries, is fundamentally different from one derived directly from a symmetry-informed magnetic structure. For, the former type of order uses nebulous loop currents circulating coherently between vanadium and ligand orbitals, whereas our magnetic order is built with local vanadium electronic multipoles with defined discrete symmetries decorating a lattice. The proposed magnetic motifs are undistorted descendants of the kagome chemical structure. Hosting a vanadium entity, defined in Sec. III A, that is a true scalar and magnetic epitomizes an absence of current loops. Likewise in the case of ceramic superconductor materials, where copper Dirac multipoles furnish a good account of magnetism in the pseudogap phase. The value of the successful analysis of a neutron Bragg diffraction pattern from Hg1201 has been bolstered by a microscopic account of the formation of the relevant magnetic order parameter [14–16]. Specifically, anti-inversion symmetry in Cu sites emerges from centrosymmetric sites in the parent chemical structure. Moreover, the Dirac dipole depicted in Fig. 1, also called an anapole or a toroidal dipole, has been directly observed in both neutron and x-ray diffractions [17,18]. The work of Fernández-Rodríguez *et al.* [18] is particularly relevant to our current story for they deployed resonant x-ray diffraction to observe the vanadium anapole in vanadium sesquioxide (V_2O_3).

II. SYMMETRY CONSIDERATIONS AND MAGNETIC MOTIFS

First, the chemical structure of the kagome metal. It incorporates a net of two regular tilings, one hexagonal and one triangular, that accommodate V_3Sb_1 with vanadium cations coordinated by octahedra of antinomy. Specifically, KV_3Sb_5 is described by the centrosymmetric space-group $P6/mmm$ (No. 191) with cell dimensions $a \approx 5.483$, $c \approx 8.954$ Å [10,13]. Ions occupy centrosymmetric sites, namely, Sb_1 1(a) D_{6h}, Sb_2 4(h) C_{3v}, V 3(f) D_{2h}, and K 1(b) D_{6h}. Vanadium ions originate the kagome network, whereas the Sb_1 ions fill the centers of the triangles. Also, V_3Sb_1 layers alternates with Sb_2 layers, resulting in a quasi-two-dimensional structure. Vectors describing the KV_3Sb_5 unit cell are $\mathbf{a} = (a, 0, 0)$, $\mathbf{b} = (1/2)\ (-a, a\sqrt{3}, 0)$, and $\mathbf{c} = (0, 0, c)$ in an orthonormal coordinate system.

Conventionally, the development of magnetic order leads to a lowering of the symmetry in the sample and the magnetic ordering pattern can be inferred by confronting experimental patterns derived by neutron diffraction (and to a minor extend also by x-ray magnetic diffraction) with a symmetry analysis in which selected elements of crystal symmetry are assumed to have disappeared. In the case of KV_3Sb_5, complete absence of conventional axial magnetic dipoles implies that any other magnetism is not visible using many experimental techniques—symmetry protects a magnetic order hidden from view. Following the mentioned experimental reports, we postulate that a presence of anti-inversion (the union of spatial and time reversals) forbids all axial magnetic moments in KV_3Sb_5 (anti-inversion occurs in 21 out of the 122 magnetic point groups). Our models of hidden magnetic order are derived from the chemical structure with exclusive deployment of vanadium Dirac multipoles. Actually, symmetry in the two models of KV_3Sb_5 protects against axial magnetic dipoles at all occupied sites, and, consequently, the models respond like a nonmagnetic material in usual experimental investigations in a laboratory environment. Furthermore, by stipulating structures harboring hidden order be direct descendants of the chemical structure, we find there are just two candidates. By not seeking alternative hidden-order structures we appeal to Occam's Razor.

Plausible magnetic motifs derived from the parent structure of KV_3Sb_5 include $P6/m'mm$ and $P6'/mmm'$ (Nos. 191.235 and 191.237 BNS [19]) selected for study. Ions in these two magnetic space groups do not possess conventional magnetism with Sb_1, V, and K ions in sites that include anti-inversion ($\bar{1}'$) and Sb_2 occupies sites with polar symmetry that prohibits axial dipoles. Spatial inversion is absent at all sites in question. Magnetic crystal classes $6/m'mm$ and $6'/mmm'$ are centrosymmetric and not compatible with ferromagnetism. Any kind of magnetoelectric (ME) effect is prohibited by symmetry in $6'/mmm'$. Likewise, a magnetochiral signal discussed in the Appendix. The magnetic motif $P6'/mmm'$ hosts a new and novel entity that is a true scalar and time odd. We can associate it with a purely imaginary charge density and a fictitious electric field that satisfies Gauss's law. A linear ME effect (EH type) is allowed by $6/m'mm$ but nonlinear types are not symmetry allowed, e.g., EHH and EEH are forbidden where E (polar and time even) and H (axial and time odd) are electric and magnetic fields, respectively. Also, the aforementioned magnetochiral signal can be different from zero. Crystal chirality does not exist in the two models of KV_3Sb_5.

For our atomic description of electronic properties, vanadium ions are assigned spherical multipoles $\langle O^K_Q \rangle$ with integer rank K and projections Q in the interval $-K \leqslant Q \leqslant K$. Cartesian and spherical components of a dipole $\mathbf{R} = (x, y, z)$, for example, are related by $x = (R_{-1} - R_{+1})/\sqrt{2}$, $y = i(R_{-1} + R_{+1})/\sqrt{2}$, $z = R_0$ [21]. A complex conjugate is defined as $\langle O^K_Q \rangle^* = (-1)^Q \langle O^K_{-Q} \rangle$, and a phase convention $\langle O^K_Q \rangle = [\langle O^K_Q \rangle' + i \langle O^K_Q \rangle'']$ for real and imaginary parts labeled by single and double primes, respectively. In which case, the diagonal multipole $\langle O^K_0 \rangle$ is purely real. Angular brackets $\langle \cdots \rangle$ denote the time average or expectation value of the enclosed tensor operator, i.e., vanadium multipoles feature in the electronic ground state of KV_3Sb_5.

To establish the experimental conditions required to validate our predictions we present amplitudes or unit-cell structure factors for resonant x-ray and magnetic neutron diffraction derived from an electronic structure factor [21]. Its generic form is identical for vanadium ions at Wyckoff position $3(f)$ in $P6/m'mm$ and $P6'/mmm'$ as we see in Eq. (A2). Different site symmetries alone account for differences in diffraction amplitudes.

Our starting point is the selection of the most appropriate reference frame to describe the symmetry properties of the V ions. Reciprocal lattice vectors are found to be $\mathbf{a}^* = (ac/2)(\sqrt{3}, 1, 0) \propto [2, 1, 0]$, $\mathbf{b}^* = (ac)(0, 1, 0) \propto [1, 2, 0]$, and $\mathbf{c}^* = \sqrt{3}(a^2/2)\,(0, 0, 1)$ all in units of $(2\pi)/v_o$ with a volume $v_o = \sqrt{3}(a^2c/2)$. Miller indices (h, k, l) are integers. Our local axes for vanadium ions labeled (ξ, η, ζ) match orthogonal vectors **a**, **b***, and **c**. Regarding site symmetries for vanadium ions, antidyad $2'_\xi$ and anti-inversion elements occur in sites $3(f)$ in the two candidate structures. Additional elements $2'_\eta$, 2_ζ and 2_η, $2'_\zeta$ for $P6/m'mm$ and $P6'/mmm'$, respectively, complete lists of site symmetries. X-ray and neutron-diffraction amplitudes for reflection vectors $(h, 0, 0)$ and $(0, 0, l)$ are very different in the two candidates as we will see.

III. RESONANT X-RAY DIFFRACTION

Valence states that accept the photoejected electron, a few eV above the Fermi level, interact with neighboring ions. In consequence, any corresponding electronic multipole is rotationally anisotropic with a symmetry corresponding to the site symmetry of the resonant ion. This anisotropy is most pronounced in the direct vicinity of an absorption edge whereas it is negligible far from the edges. Nonresonant ions can be neglected in calculations of forbidden reflection structure factors to a good approximation. There are many reported examples of Bragg diffraction enhanced by absorption at the K edge of a $3d$ transition ion. Results on haematite (Fe^{3+}, $3d^5$) reported by Finkelstein *et al.* [22] are thoroughly discussed by Carra and Thole [23], whereas diffraction patterns gathered at a later date revealed a chirality [24]. The time between the publications saw reports of diffraction patterns enhanced by nickel and vanadium K edges [18,25–27].

Absorption at the K edge and an electric dipole event ($E1$) gives access to valence states with atomic p-like character, and an electric quadrupole event ($E2$) at the same edge gives access to d-like states ($1s \rightarrow 3d$). Bragg diffraction from V_2O_3 enhanced by the pre-edge ≈5.464 keV (wavelength $\lambda \approx 2.27$ Å) feature of the vanadium K shell has been successfully analyzed using the electric dipole- electric quadrupole ($E1$-$E2$) absorption event [18,28]. With an x-ray wavelength $\lambda \approx 2.27$ Å, Bragg angles in Fig. 2 are determined by $\sin(\theta) = (h\lambda)/(a\sqrt{3}) \approx (h\,0.239)$ and $\sin(\theta) = (l\lambda)/(2c) \approx (l\,0.127)$ for reflection vectors $(h, 0, 0)$ and $(0, 0, l)$, respectively. The triangle rule says that multipoles possess ranks K = 1–3 for this parity-odd event [21,29]. Dipoles (K = 1) in the parity-even $E1$-$E1$ absorption event are magnetic, and irrelevant to our study of KV_3Sb_5. First, parity-even (axial) magnetic multipoles do not exist at sites that contain anti-inversion, and such is the case for Sb_1, V, and K ions. Second, axial dipoles do not exist at sites $4(h)$ used by Sb_2. However, a parity-even quadrupole and octupoles (K = 3) with projections $Q = \pm 3$ are permitted by $4(h)$ symmetry. The Sb multipoles would contribute to diffraction enhanced by a Sb $E1$-$E1$ or $E2$-$E2$ absorption events, but it does not exist at the vanadium K edge of interest here. To summarize, vanadium diffraction patterns presented below exist with broken time-reversal symmetry, polar magnetism, and concomitant vanadium Dirac multipoles. We focus on x-ray amplitudes in which polarization is rotated, e.g., $\sigma \rightarrow \pi'$ in Fig. 2 for Thomson scattering is absent in the rotated channel of polarization. In the nominal setting of the crystal (ξ, η, ζ) coincide with (x, y, z) in Fig. 2, which depicts four states of x-ray polarization.

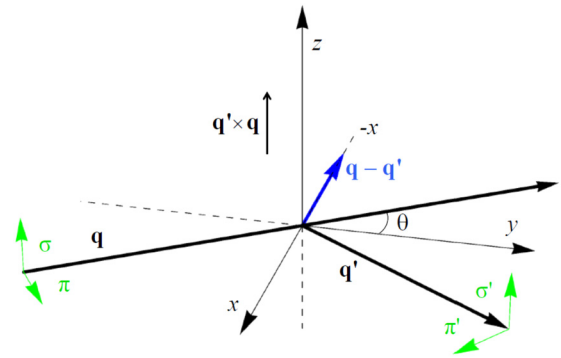

FIG. 2. Primary (σ, π) and secondary (σ', π') states of polarization. Corresponding wave-vectors **q** and **q**' subtend an angle 2θ. The Bragg condition for diffraction is met when $\mathbf{q} - \mathbf{q}'$ coincides with the reflection vector indexed (h, k, l). Crystal vectors **a**, **b***, and **c** that define (ξ, η, ζ) and depicted Cartesian (x, y, z) coincide in the nominal setting of the crystal.

A resonant atomic process may dominate all other contributions to the x-ray scattering length should the photon energy E match a resonance energy Δ. Assuming virtual intermediate states in the process are spherically symmetric, to a good approximation, the x-ray scattering length $\approx \{(\mu\eta)/(E - \Delta + i\Gamma/2)\}$ in the region of the resonance, where Γ is the total width of the resonance [21]. The numerator $(\mu\eta)$ is an amplitude or unit-cell structure factor for Bragg diffraction in the scattering channel with primary (secondary) polarization $\eta(\mu)$. By convention, σ denotes polarization normal to the plane of scattering, and π denotes polarization within the plane of scattering as in Fig. 2. The illuminated crystal is rotated about the reflection vector in an azimuthal angle scan. Intensity of a Bragg spot in the $\sigma \rightarrow \pi'$ channel of polarization is proportional to $|(\pi'\sigma)|^2$ and likewise for unrotated channels of polarization.

A signature of crystal chirality is the difference between Bragg intensities measured with left- and right-handed primary x-rays, or x-rays with opposite helicities. A relevant quantity Υ depends on all four scattering amplitudes $\Upsilon = \{(\sigma'\pi)^*(\sigma'\sigma) + (\pi'\pi)^*(\pi\sigma)''\}$. Specifically, crystal chirality means an intensity $P_2\Upsilon$ different from zero where the Stokes parameter P_2 (a purely real pseudoscalar) measures helicity in the primary x-ray beam. Since intensity is a true scalar, Υ and P_2 must possess identical discrete symmetries, specifically, both scalars are time even and parity odd. The chiral signature Υ for vanadium ions is zero for all Bragg diffraction patterns that we choose to discuss.

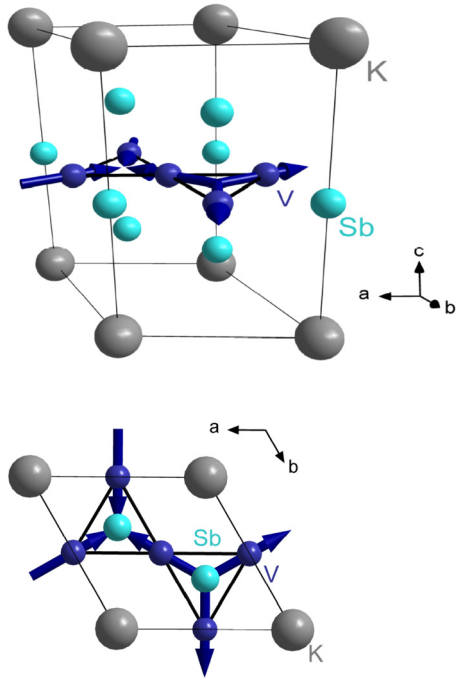

FIG. 3. Anapole motif in $P6'/mmm'$ (No. 1911. 237) viewed in two perspectives. They are depicted in Fig. 1 and are represented here by dark blue arrows. Two anapoles are normal to the crystal **a** axis and parallel to hexagonal $[1, 2, 0] \propto \mathbf{b}^*$ in the bottom panel. Cell vectors **a** and **b** subtend an angle 120° (Sec. II). Light blue and gray spheres represent Sb and K ions, respectively.

In the following, we give explicit expressions for scattering amplitudes for the two models: (A) $P6'/mmm'$ with any kind of ME effect prohibited by symmetry in $6'/mmm'$, and (B) $P6/m'mm$ with a linear ME effect permitted by $6/m'mm$. All reported x-ray scattering amplitudes are derived from universal expressions for diffraction by Dirac multipoles visible in x-ray scattering enhanced by an $E1$-$E2$ absorption event [29].

A. $P6'/mmm'$ (nonmagnetoelectric)

In this model, sites $3(f)$ used by V ions possess symmetry mmm'. Projections Q on Dirac multipoles $\langle \mathrm{G}^{\mathrm{K}}{}_Q \rangle$ are odd by virtue of the antidyad $2'_\zeta$ in the symmetry elements of the point group, and, consequently, magnetic charge $\langle G^0 \rangle$ is not allowed. In addition, symmetry $2'_\xi$ is satisfied by $\langle G^{\mathrm{K}}_{-Q} \rangle = (-1)^{\mathrm{K}+1} \langle G^{\mathrm{K}}_Q \rangle$ that leads to the identity $\langle G^{\mathrm{K}}_Q \rangle^* = (-1)^{\mathrm{K}} \langle G^{\mathrm{K}}_Q \rangle$ for Q odd. Anapoles $\langle \mathbf{G}^1 \rangle$ depicted in Fig. 3 are parallel to the reciprocal vector $\mathbf{b}^*$, i.e., the local η axis.

Inspection of Fig. 3 reveals a strange entity at the midpoint of each triangle with antimony ions displaced above and below the plane of the triangle. The entity is a true scalar and time odd. Whereas, a like entity created with axial dipoles is a Dirac monopole that can be accommodated in Maxwell's equations of electrodynamics. We equate the entity with $i\rho$, where ρ is a purely real charge density. This line of argument uses the fact that time reversal includes the operation of complex conjugation [30]. Upon associating ρ with charge a conjugate (fictitious) field **E** satisfies div $\mathbf{E} = \rho$ (Gauss's law), and its magnitude as a function of distance obeys an inverse square law.

Evaluated for $(0, 0, l)$, the unit-cell structure factor Eq. (A2) is proportional to $[1 + 2\cos(2\pi Q/3)]$ that is zero for projections $Q = \pm 1$. Projections $Q = \pm 3$ are allowed, however, and can only belong to an octupole accessed in the $E1$-$E2$ absorption event (K = 3). Amplitudes of diffraction in rotated channels of polarization $(\pi'\sigma)$ and $(\sigma'\pi)$, and a Bragg spot $(0, 0, l)$ are as follows:

$$(\pi', \sigma) = -(\sigma'\pi) = 3\,\sin(2\theta)\sin(3\psi)\langle G^3_{+3}\rangle'', \quad (0, 0, l). \tag{1}$$

Here, θ is the Bragg angle depicted in Fig. 2, and ψ is the angle of rotation of the crystal around the reflection vector $(0, 0, l)$. At the azimuthal origin $\psi = 0$ the crystal **a** axis is normal to the plane of scattering in Fig. 2. Notable features of amplitudes in Eq. (1) include a threefold periodicity in ψ from the tertiary axis of rotation symmetry, sole dependence on a lone octupole, and handedness observed in the sign difference between $(\pi'\sigma)$ and $(\sigma'\pi)$. Amplitudes in unrotated channels of polarization are significantly different with respect to ψ. For example,

$$(\sigma'\sigma) = -(3/2)\cos(\theta)[19\,\cos(3\psi) + \cos(\psi)]\langle G^3_{+3}\rangle'', \quad (0, 0, l). \tag{2}$$

Amplitudes $(\sigma'\sigma)$ and $(\pi'\sigma)$ have opposite trends with respect to increasing l and are even and odd functions of ψ, respectively.

Amplitudes $(\sigma'\sigma)$ and $(\pi'\pi)$ for a reflection vector $(h, 0, 0)$ are zero. Amplitudes $(\pi'\sigma)$ and $(\sigma'\pi)$ can be nonzero, however, and they are different for h odd and h even. First, h even amplitudes depend on the octupole visible in $(0, 0, l)$ Bragg spots, namely,

$$(\pi'\sigma) = (\sigma'\pi) = -3\,\cos^2(\theta)\sin(2\psi)\langle G^3_{+3}\rangle'', \quad (2n, 0, 0). \tag{3}$$

The crystal **c** axis is normal to the plane of scattering for $\psi = 0$. Amplitudes for h odd engage another three multipoles yet possess the dependence on θ and ψ displayed in Eq. (3). Additional multipoles are $\langle G^2_{+1}\rangle'$, $\langle G^3_{+1}\rangle''$, and $\langle G^3_{+3}\rangle''$.

B. $P6/m'mm$ (magnetoelectric)

Sites $3(f)$ occupied by V ions possess symmetry $m'mm$. Projections on Dirac multipoles $\langle G^{\mathrm{K}}_Q \rangle$ are even by virtue of the dyad 2_ζ, meaning $Q = 0, \pm 2$ for an $E1$-$E2$ absorption event with $\mathrm{K} = 1, 2, 3$. The anapole $\langle G^1_0 \rangle$ is parallel to the hexagonal axis **c**, and the ferromotif is depicted in Fig. 4. Results $\langle G^{\mathrm{K}}_{-Q} \rangle = (-1)^{\mathrm{K}+1} \langle G^{\mathrm{K}}_Q \rangle$ and $\langle G^{\mathrm{K}}_Q \rangle^* = -(-1)^{\mathrm{K}} \langle G^{\mathrm{K}}_Q \rangle$ follow from the symmetry element $2'_\xi$. Like the non-ME motif, magnetic charge $\langle G^0 \rangle$ is prohibited. All $P6/m'mm$ scattering amplitudes are zero for Bragg spots $(0, 0, l)$, however, whereas like spots offer a direct test on the existence of $\langle G^3_{+3}\rangle''$ in the other candidate structure.

Turning to $(h, 0, 0)$ and h even,

$$\begin{aligned}(\pi'\sigma) &= -(\sigma'\pi) \\ &= \sin(2\theta)\cos(\psi)\{\sqrt{6}\langle G^1_0\rangle - [5\,\cos(2\psi) - 3]\langle G^3_0\rangle\}, \\ &\quad (2n, 0, 0).\end{aligned} \tag{4}$$

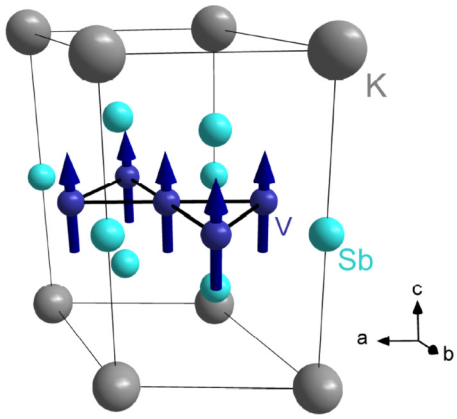

FIG. 4. Ferromotif of anapoles in $P6/m'mm$ (No. 191.235). Cell vectors **a** and **b** subtend an angle 120° (Sec. II). Light blue and gray spheres represent antimony and potassium ions, respectively.

Notably, only diagonal multipoles ($Q = 0$) contribute, including the anapole parallel to the crystal **c** axis. With regard to a dependence on the azimuthal angle, $\cos(\psi)$ identifies $[\langle G_0^1\rangle + \sqrt{(3/2)}\langle G_0^3\rangle]$ and $\cos(\psi)\cos(2\psi)$ identifies $\langle G_0^3\rangle$, i.e., the two contributing multipoles can be separated in an analysis of experimental data. Similar results are obtained for unrotated amplitudes, e.g.,

$$(\sigma'\sigma) = -2\cos(\theta)\sin(\psi)\left\{\sqrt{6}\langle G_0^1\rangle + [5\cos(2\psi)+3]\langle G_0^3\rangle\right\}, \quad (2n,\,0,\,0). \tag{5}$$

There are an additional two multipoles in amplitudes with h odd. Specifically,

$$(\pi'\sigma) = -(\sigma'\pi) = (2/3)\sqrt{(5/3)}\sin(2\theta)\cos(\psi) \times \left\{-\sqrt{(3/20)}\left[\sqrt{6}\langle G_0^1\rangle - (5\cos(2\psi)-3)\langle G_0^3\rangle\right] - 4\langle G_{+2}^2\rangle'' + \sqrt{2}(3\cos(2\psi)-1)\langle G_{+2}^3\rangle'\right\}, \quad (2n+1,\,0,\,0). \tag{6}$$

The $(\sigma'\sigma)$ amplitude is composed of the same multipoles, and $\cos(\theta)\,\sin(\psi)$ multiplies and even function of ψ. Thus, for $h = 2n+1$, amplitudes $(\sigma'\sigma)$ and $(\pi'\sigma)$ are odd and even functions of ψ, respectively.

IV. MAGNETIC NEUTRON DIFFRACTION

A magnetic scattering amplitude $\langle \mathbf{Q}_\perp\rangle$ generates an intensity $|\langle \mathbf{Q}_\perp\rangle|^2$ of unpolarized neutrons. Dirac multipoles contribute to scattering, and each one is accompanied by an atomic form factor that depends on the magnitude of the reflection vector and the electronic configuration [31].

Polarization analysis measures the magnetic content of a Bragg spot with overlapping nuclear and magnetic amplitudes, which occurs when the magnetic motif and chemical structure coincide [16,20]. Primary and secondary polarizations are denoted **P** and **P′**, and a fraction $(1 - \mathbf{P}\cdot\mathbf{P}')/2$ of neutrons participate in events that change (flip) the neutron spin orientation. For a collinear magnetic motif one finds $(1 - \mathbf{P}\cdot\mathbf{P}')/2 \propto \{(1/2)(1+\mathrm{P}^2)|\langle \mathbf{Q}_\perp\rangle|^2 - |\mathbf{P}\cdot\langle \mathbf{Q}_\perp\rangle|^2\}$. A quantity called spin flip,

$$(\mathrm{SF}) = \{|\langle \mathbf{Q}_\perp\rangle|^2 - |\mathbf{P}\cdot\langle \mathbf{Q}_\perp\rangle|^2\} \tag{7}$$

obtained with $P^2 = 1$ is a standard measure of the strength of magnetic scattering [16].

A Dirac dipole $\langle \mathbf{D}\rangle$ in neutron diffraction is the sum of three contributions that include expectation values of spin and orbital anapoles. Electronic spin, orbital angular momentum, and position operators are **S**, **L** and **R**, respectively. Operators for the three contributions to **D** are a spin anapole (**S** × **R**), orbital anapole $\mathbf{\Omega} = [\mathbf{L}\times\mathbf{R} - \mathbf{R}\times\mathbf{L}]$, and $(i\mathbf{R})$. Specifically, $\langle \mathbf{D}\rangle = (1/2)[3(h_1)\langle(\mathbf{S}\times\mathbf{R})\rangle - (j_0)\langle\mathbf{\Omega}\rangle + (g_1)\langle(i\mathbf{R})\rangle]$. Form factors (h_1), (j_0) and (g_1) have been calculated for several atomic configurations [32,33]. In what follows, we retain $\langle \mathbf{D}\rangle$ and a quadrupole $\langle \mathbf{H}^2\rangle$ that possess the largest atomic form factors. A quadrupole of this type is a product of (h_1) and a correlation function $\langle\{\mathbf{S}\otimes\mathbf{R}\}^2\rangle$ written in terms of a standard tensor product of two dipoles [31]. Notably, $\langle \mathbf{H}^2\rangle \propto [(h_1)\langle\{\mathbf{S}\otimes\mathbf{R}\}^2\rangle]$ accounts for magnetic neutron diffraction by the pseudogap phase of ceramic superconductors [20].

A. $P6'/mmm'$ (nonmagnetoelectric)

The motif of anapoles is depicted in Fig. 3. No diffraction takes place with anapoles and quadrupoles at Bragg spots indexed by $(0, 0, l)$. Likewise, for $(h, 0, 0)$ with $h = 2n$. Amplitudes for $(h, 0, 0)$ with Miller index h odd are $\langle Q_{\perp\xi}\rangle \approx 0$, $\langle Q_{\perp\eta}\rangle \approx 0$, and,

$$\langle Q_{\perp\zeta}\rangle \approx i\left[-\langle \mathrm{D}_\eta\rangle + (3/\sqrt{5})\left\langle \mathrm{H}_{+1}^2\right\rangle'\right], \quad (2n+1,\,0,\,0). \tag{8}$$

The dipole contribution is parallel to the reciprocal vector $\mathbf{b}^*$. From Eqs. (7) and (8), (SF) = 0 for polarization **P** parallel to the crystal **c** axis, whereas $(\mathrm{SF}) = |\langle \mathbf{Q}_\perp\rangle|^2$ for **P** in the basal plane.

B. $P6/m'mm$ (magnetoelectric)

As with the motif depicted in Fig. 3, there is no diffraction at Bragg spots indexed by $(0, 0, l)$ in the ferro-type motif depicted in Fig. 4. However, diffraction at Bragg spots $(h, 0, 0)$ occurs at both h even and h odd. One finds, $\langle \mathrm{Q}_{\perp\xi}\rangle \approx 0$, $\langle \mathrm{Q}_{\perp\zeta}\rangle \approx 0$ and

$$\langle Q_{\perp\eta}\rangle \approx i\left[\langle \mathrm{D}_\zeta\rangle - (3/\sqrt{5})\left\langle \mathrm{H}_{+2}^2\right\rangle''\right], \quad (2n+1,\,0,\,0) \tag{9}$$

for h odd. The quadrupole in Eq. (9) is absent for $h = 2n$. Evidently, $(\mathrm{SF}) = |\langle \mathbf{Q}_\perp\rangle|^2$ for **P** parallel to either [2, 1, 0] or [0, 0, 1] crystal axes, whereas (SF) = 0 for **P** parallel to the crystal $\mathbf{b}^*$ axis.

V. CONCLUSIONS

In summary, we have studied two models of a magnetic material on a kagome lattice with a view to interpreting enigmatic properties of KV_3Sb_5 at a low temperature. Their distinguishing features are a complete absence of conventional (axial, parity-even) magnetic dipoles, and a lattice structure that is a direct descendent of the kagome chemical structure. The latter feature is self-evident in the specification of the models by magnetic space groups $P6'/mmm'$ and $P6/m'mm$ derived from the kagome structure $P6/mmm$.

Anapole motifs are shown in Figs. 3 and 4. Magnetic properties of the models chime with the absence in KV_3Sb_5 of magnetic long-range order and, also, a vanadium magnetic moment in available measurements [10,12].

Symmetry in the form of anti-inversion, the union of space and time inversions, prohibits all axial vanadium magnetic multipoles. Magnetism exists in the form of vanadium Dirac multipoles that are magnetic and polar. A vivid portrayal of the unconventional nature of the magnetism is the existence of a magnetic true scalar in one model ($P6'/mmm'$, Sec. III A and Fig. 3). The strange entity formed with anapoles has not been identified in the past to the best of our knowledge. It is associated with a charge distribution that is purely imaginary. Notably, a like entity formed with axial dipoles is the familiar Dirac monopole that finds a place in Maxwell's equations of electrodynamics [34]. Dirac multipoles deflect neutrons and x rays so future Bragg diffraction experiments using these radiations can inform us whether the models we have studied are noteworthy. To this end, scattering amplitudes for neutron diffraction and x-ray diffraction with signal enhancement by a vanadium atomic resonance are reported. Resonant x-ray Bragg diffraction by vanadium Dirac dipoles, also called anapoles (Fig. 1), has previously been identified in the diffraction pattern of V_2O_3 [18]. In addition, there is direct evidence of neutron scattering by anapoles [17].

Our two models possess different megnetoelectric (ME) properties. Any type of ME effect is prohibited in $P6'/mmm'$, whereas a linear ME effect is permitted in $P6/m'mm$. Vanadium magnetic monopoles (Dirac scalars) are forbidden in both models. Anapoles are aligned with $\mathbf{b}^*$ ($\mathbf{c}$) in $P6'/mmm'$ ($P6/m'mm$), where the reciprocal lattice vector $\mathbf{b}^*$ is orthogonal to lattice vectors $\mathbf{a}$ and $\mathbf{c}$ in Figs. 3 and 4. As an example of how neutron Bragg diffraction can be used to differentiate between the two models, we mention the spin-flip signal reported in Sec. IV. In brief, the signal is zero for neutron polarization parallel to the crystal $\mathbf{b}^*$ ($\mathbf{c}$) axis for $P6/m'mm$ ($P6'/mmm'$). Regarding resonant x-ray diffraction with signal enhancement by an electric dipole - electric quadrupole ($E1$-$E2$) event at the vanadium K edge, Bragg spots are allowed for a reflection vector parallel to the c axis in $P6'/mmm'$, whereas no such Bragg spots are allowed in $P6/m'mm$. Section III includes scattering amplitudes for a reflection vector on the basal plane. As for bulk responses, natural circular dichroism is forbidden in both models. A magnetochiral signal is permitted for $P6/m'mm$ but not for $P6'/mmm'$.

Sites 4(h) used by Sb_2 in our models do not contain anti-inversion or inversion symmetries. In the absence of anti-inversion conventional magnetism (parity $\sigma_\pi = +1$) is not forbidden, unlike all other sites in our two models of KV_3Sb_5, and might arise from backelectron transfer. For completeness, we survey the multipoles $\langle \mathrm{O}^{\mathrm{K}}_Q \rangle$ of rank K allowed by site symmetries. For sites 4(h) they are 3_ζ, $m_\xi = I2_\xi$ and $\langle \mathrm{O}^{\mathrm{K}}_Q \rangle = (-1)^Q \exp(-i\pi Q/3)[m_\xi \langle \mathrm{O}^{\mathrm{K}}_Q \rangle]$ leading to projections $Q = 3n$ and $\langle \mathrm{O}^{\mathrm{K}}_Q \rangle = \sigma_\pi (-1)^{\mathrm{K}+Q} \langle \mathrm{O}^{\mathrm{K}}_Q \rangle^*$. Orthogonal crystal vectors $\mathbf{a}$, $\mathbf{b}^*$, and $\mathbf{c}$ define (ξ, η, ζ). Allowed parity-even magnetism includes multipoles $\langle T^2_0 \rangle$ and $\langle T^3_{+3} \rangle'$, and associated magnetic fields might be sensed in zero-field μSR. Both multipoles contribute to neutron scattering, whereas just $\langle T^3_{+3} \rangle'$ can be seen in a parity-even absorption event, namely, $E2$-$E2$. Dirac multipoles permitted in neutron scattering and an $E1$-$E2$ absorption event include an anapole $\langle G^1_0 \rangle$ and octupoles $\langle G^3_0 \rangle$, and $\langle G^3_{+3} \rangle''$.

Anti-inversion symmetry at sites used by vanadium ions is the key component of our filter of magnetic models that descend from the kagome lattice. Absence by symmetry of axial magnetic dipoles at all sites used by the three elements in KV_3Sb_5 is a further requirement. The second component eliminates $P6'/mm'm$ (No. 191.236 [19]) and $P6/m'm'm'$ (No. 191.241) as acceptable models because magnetic dipoles are permitted at sites 4(h). According to conventional displays of magnetic space groups our two magnetic models of KV_3Sb_5 are actually classified as nonmagnetic.

APPENDIX

An electronic structure factor,

$$\Psi^{\mathrm{K}}_Q = \left[\exp(i\boldsymbol{\kappa} \cdot \mathbf{d}) \langle \mathrm{O}^{\mathrm{K}}_Q \rangle_{\mathbf{d}}\right], \tag{A1}$$

where the reflection vector $\boldsymbol{\kappa}$ is defined by Miller indices (h, k, l), and the implied sum is over three vanadium ions in sites $\mathbf{d}$, 3(f). For candidates $P6/m'mm$ and $P6'/mmm'$ (Nos. 191.235 and 191.237 [19]),

$$\Psi^{\mathrm{K}}_Q(3f) = \langle \mathrm{O}^{\mathrm{K}}{}_Q \rangle \left[(-1)^h + (-1)^{h+k} \gamma_Q{}^* + (-1)^k \gamma_Q\right], \tag{A2}$$

with $\gamma_Q = \exp(i2\pi Q/3)$ and reference site (1/2, 0, 0) for $\langle \mathrm{O}^{\mathrm{K}}_Q \rangle$. Our two candidates differ with respect to site symmetries that delineate properties of $\langle \mathrm{O}^{\mathrm{K}}_Q \rangle$, namely, mmm' (No. 191.237) or $m'mm$ (No. 191.235).

Natural circular dichroism is forbidden by anti-inversion in the symmetry of sites occupied by vanadium ions. Other bulk properties are described by Eq. (A2) evaluated for the forward direction of scattering. Miller indices are zero, and $\Psi^{\mathrm{K}}_Q(3f) = \langle \mathrm{O}^{\mathrm{K}}_Q \rangle \ [1 + 2\cos(2\pi Q/3)] = 3 \ \langle \mathrm{O}^{\mathrm{K}}_Q \rangle$ for $Q = 3n$ and zero otherwise. With an $E1$-$E2$ absorption event and the x-ray beam parallel to the crystal c axis the magnetochiral signal is proportional to $[\langle G^1_0 \rangle - \sqrt{(2/3)} \langle G^3_0 \rangle]$, which is permitted for $P6/m'mm$ but not for $P6'/mmm'$ [21,35].

Scattering amplitudes in Refs. [29,31] used here are functions of two quantities, one even and one odd with respect to the sign of Q. For neutron scattering $A^{\mathrm{K}}_Q \pm B^{\mathrm{K}}_Q = \Psi^{\mathrm{K}}_{\pm Q}$ [31]. In the case of x-ray diffraction, it is necessary to align the reflection vector $\boldsymbol{\kappa}$ with the $-x$ axis depicted in Fig. 2. For reflections (h, 0, 0), the result is $A^{\mathrm{K}}_Q \pm B^{\mathrm{K}}_Q = \exp(\pm iQ\alpha) \ \Psi^{\mathrm{K}}_{\pm Q}$ with angle $\alpha = -30^\circ$. The corresponding result for a reflection vector (0, 0, l) is more complicated, and it can be found in Eq. (104) in Ref. [21].

[1] J. G. Bednorz and K. A. Müller, Z. Phys. B: Condens. Matter **64**, 189 (1986).

[2] R. B. Laughlin, Phys. Rev. B **89**, 035134 (2014).

[3] X. Zhou, W-S. Lee, M. Imada, N. Trivedi, P. Phillips, H-Y. Kee, P. Törmä, and M. Eremets, Nat. Rev. Phys. **3**, 462 (2021).

[4] C. M. Varma, Phys. Rev. B **55**, 14554 (1997).
[5] S. Chakravarty, R. B. Laughlin, D. K. Morr, and C. Nayak, Phys. Rev. B **63**, 094503 (2001).
[6] F. D. M. Haldane, Phys. Rev. Lett. **61**, 2015 (1988).
[7] Y. -X. Jiang *et al.*, Nat. Mater. **20**, 1353 (2021); X. Feng, K. Jiang, Z. Wang, and J. Hu, Sci. Bull. **66**, 1384 (2021).
[8] Q. Yin, Z. Tu, C. Gong, Y. Fu, S. Yan, and H. Lei, Chin. Phys. Lett. **38**, 037403 (2021).
[9] B. R. Ortiz, S. M. L. Teicher, Y. Hu, J. L. Zuo, P. M. Sarte, E. C. Schueller, A. M. M. Abeykoon, M. J. Krogstad, S. Rosenkranz, R. Osborn, R. Seshadri, L. Balents, J. He, and S. D. Wilson, Phys. Rev. Lett. **125**, 247002 (2020).
[10] B. R. Ortiz, L. C. Gomes, J. R. Morey, M. Winiarski, M. Bordelon, J. S. Mangum, I. W. H. Oswald, J. A. Rodriguez-Rivera, J. R. Neilson, S. D. Wilson, E. Ertekin, T. M. McQueen, and E. S. Toberer, Phys. Rev. Materials **3**, 094407 (2019).
[11] B. R. Ortiz, P. M. Sarte, E. M. Kenney, M. J. Graf, S. M. L. Teicher, R. Seshadri, and S. D. Wilson, Phys. Rev. Materials **5**, 034801 (2021).
[12] E. M. Kenney, B. R. Ortiz, C. Wang, S. D. Wilson, and M. J. Graf, J. Phys.: Condens. Matter **33**, 235801 (2021).
[13] C. Mielke III *et al.*, Nature (London) **602**, 245 (2022); commentary, M. H. Christensen, and T. Birol, *ibid.* **602**, 216 (2022).
[14] S. W. Lovesey and D. D. Khalyavin, J. Phys.: Condens. Matter **29**, 215603 (2017).
[15] M. Fechner, M. J. A. Fierz, F. Thöle, U. Staub, and N. A. Spaldin, Phys. Rev. B **93**, 174419 (2016).
[16] P. Bourges, D. Bounoua, and Y. Sidis, C. R. Phys. **22**, 1 (2021).
[17] S. W. Lovesey, T. Chatterji, A. Stunault, D. D. Khalyavin, and G. van der Laan, Phys. Rev. Lett. **122**, 047203 (2019).
[18] J. Fernández-Rodríguez, V. Scagnoli, C. Mazzoli, F. Fabrizi, S. W. Lovesey, J. A. Blanco, D. S. Sivia, K. S. Knight, F. de Bergevin, and L. Paolasini, Phys. Rev. B **81**, 085107 (2010).
[19] We use the BNS setting of magnetic space groups, see Bilbao Crystallographic server, https://www.cryst.ehu.es./.
[20] S. W. Lovesey and D. D. Khalyavin, J. Phys.: Condens. Matter **27**, 495601 (2015).
[21] S. W. Lovesey, E. Balcar, K. S. Knight, and J. Fernández Rodríguez, Phys. Rep. **411**, 233 (2005).
[22] K. D. Finkelstein, Q. Shen, and S. Shastri, Phys. Rev. Lett. **69**, 1612 (1992).
[23] P. Carra and B. T. Thole, Rev. Mod. Phys. **66**, 1509 (1994).
[24] J. Fernández-Rodríguez, S. W. Lovesey, and J. A. Blanco, Phys. Rev. B **77**, 094441 (2008).
[25] J. P. Hill, C. -C. Kao, and D. F. McMorrow, Phys. Rev. B **55**, R8662 (1997).
[26] L. Paolasini, C. Vettier, F. de Bergevin, F. Yakhou, D. Mannix, A. Stunault, W. Neubeck, M. Altarelli, M. Fabrizio, P. A. Metcalf, and J. M. Honig, Phys. Rev. Lett. **82**, 4719 (1999).
[27] S. W. Lovesey and K. S. Knight, J. Phys.: Condens. Matter **12**, L367 (2000).
[28] S. W. Lovesey, J. Fernández-Rodríguez, J. A. Blanco, D. S. Sivia, K. S. Knight, and L. Paolasini, Phys. Rev. B **75**, 014409 (2007).
[29] V. Scagnoli and S. W. Lovesey, Phys. Rev. B **79**, 035111 (2009).
[30] B. A. Bernevig, with and T. L. Hughes, *Topological Insulators and Topological Superconductors* (Princeton University Press, Princeton, 2013).
[31] S. W. Lovesey, Phys. Scr. **90**, 108011 (2015).
[32] S. W. Lovesey, J. Phys.: Condens. Matter **26**, 356001 (2014).
[33] G. van der Laan and S. W. Lovesey, Phys. Rev. B **103**, 125124 (2021).
[34] K. A. Milton, Rep. Prog. Phys. **69**, 1637 (2006).
[35] S. W. Lovesey and E. Balcar, Phys. Scr. **81**, 065703 (2010).